cemented specimens were clearly separated into a cement part (Zn-rich area) and an YPSZ area (Zr-rich area). The cement-YPSZ boundary was clear, and interface fracture between YPSZ and zinc phosphate cement was suggested. In contrast, the glass ionomer- and adhesive resin composite cement-bonded specimens showed complex, intricate surfaces, implying partly cohesive fracture.

DISCUSSION

In this study, the effects on shear bond strength of various surface conditions of YPSZ in combination with various cements were investigated. The bonding strength of YPSZ with two different surface roughnesses and three types of cement was tested. It was found that different surface roughnesses did not influence bonding strength, whereas different types of silanization and cement used significantly affected the bonding strength of the adhesive resin composite cement. In all surface pretreatments, the shear bond strength increased in the order of adhesive resin composite cement > glass ionomer cement > zinc phosphate cement.

In a previous report, the authors investigated the bonding strength of YPSZ using threaded and tapered holes in a brass plate and YPSZ milled specimens[11]. In that study[11], the glass ionomer cement showed the highest bonding strength, whereas no significant differences were seen between adhesive resin composite and zinc phosphate cements[11]. In contrast, in the present study, the adhesive resin composite cement showed the highest bonding strength. Differences in the test methods were considered to be one possible cause for the different results obtained in the two studies. In the previous study[11], the specimens and the brass plate were tapered. Therefore, the applied force probably included not only the shearing force, but also tensile force. In addition, when luted with the various cements studied, the YPSZ specimens were placed manually in drilled tapered holes[11]. This might have resulted in cement layers with inconsistent thicknesses. With the present method, the flat surface of an YPSZ specimen was bonded to another surface with a similar surface condition, and hence the bonding condition was reproduced more consistently than the previous method. In the present study, the shear force was applied in a direction perpendicular to the bonding plane. The present method should, therefore, more accurately determine the bonding strength to YPSZ of the three types of cement studied.

Compared to the other surface treatment, MPTS treatment when used in conjunction with the adhesive resin cement yielded a higher shear bond strength — but their difference was of low significance ($0.1>p>0.05$). The reason for the difference in bonding effectiveness between MPTS and PBA was considered to be as follows. In the PBA treatment, a mixture of PBA and the primer (Clearfil Linerbond IIS) was applied on the YPSZ surface and air-dried. In contrast, the MPTS treatment was carried out at 60℃ and drying was done in a vacuum after removing the residual MPTS-toluene solution. Therefore, the formed surface layer would be thinner and more tightly bonded to the YPSZ surface than with the PBA pretreatment. Thus, results in the present study indicated that the combination of adhesive

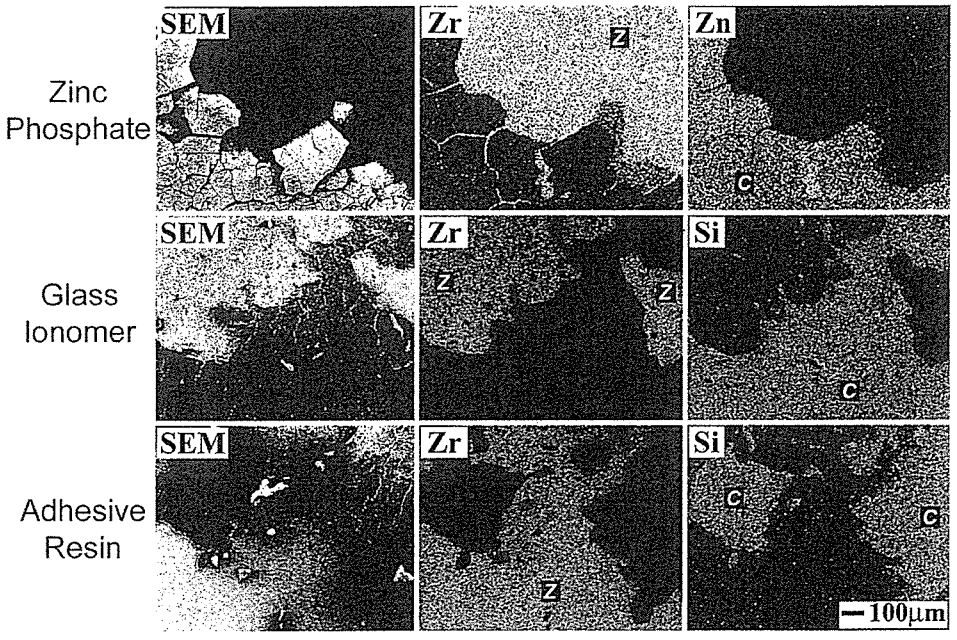

Fig. 5 SEM and elemental distribution images of fractured surfaces bonded with the three cements studied (C: cement, Z: YPSZ).

resin composite cement with MPTS pretreatment produced a more effective bonding to YPSZ than the combination with PBA treatment.

In previous studies, bonding strengths of various adhesive resin luting agents to zirconia ceramic specimens were reported to range between 1.7 and 70.4 MPa[17,20]. In most of the studies that addressed the bonding strength to zirconia ceramics, the specimens were made out of homogenous ceramic green-body blanks of zirconia, and various bonding systems and pretreatments were used[13-19]. In the current study, specimens of high-density, sintered, prefabricated zirconia blanks – called hot isostatically pressed (HIPed) zirconia blanks – were used. In an earlier report on the bonding strength of HIPed YPSZ[11], the mean values were 12 MPa for adhesive resin composite cement, 21 MPa for glass ionomer cement, and 9 MPa for zinc phosphate cement. In other words, the mean value of the adhesive resin composite cement was close to the value obtained in the current study, whereas the values obtained for zinc phosphate and glass ionomer cements were lower.

The effects of surface treatment on bonding to dental ceramics other than zirconia have also been presented in earlier studies[12,21-24]. For example, the shear bond strengths of adhesive resin composite cement with the silanized surface of lithium disilicate glass-ceramics and feldspar ceramics have been reported to be 47 MPa for Empress 2[12] (Ivoclar Vivadent, Schaan, Lichtenstein), 18 MPa for Vita VMK 68[22], 42 MPa for Cerec Vitablocs Mark II[23], and 55 MPa for Vita Celay[24] (all Vita products from Vita Zahnfabrik, Bad Säckingen, Germany). Aida *et al.* reported that the bonding strength of another feldspar ceramic (Laminabond Porcelain, Shofu, Kyoto, Japan) increased with silanization treatment when using commercial priming silane agents other than MPTS[21]. These herein-mentioned results contradicted partially with the results obtained in the present study. Disagreements could be due to differences in the silane treatment and the ceramics used. In terms of silanization, it should be noted that hydrofluoric acid etching of conventional silica-based ceramics usually improves the effects of silanization and adhesive bonding[12], whereas dental zirconia ceramics are unetchable with hydrofluoric acid. However, it has been said that the phosphate ester group in the Panavia 21 resin composite bonds directly to metal oxides[26] and chemically to zirconia ceramics[12].

Thus far, it can be seen that the reported bonding strengths of cements to dental ceramics vary widely, making it difficult to assess their clinical significance. It has been suggested that 10-13 MPa is the minimum strength needed for clinical bonding[27,28]. On the other hand, the *in vitro* bond strengths to acid-etched human dentin of various commercial resin composite bonding cements, which have been in clinical use for a relatively long time, were reported to range from 1.1 to 14.8 MPa[29]. For conventional zinc phosphate cement, Øilo[30] reported a tensile bond strength of 0.6 MPa to dentin and Richardson *et al.* 0.9 MPa[31]. Although those values seem to be very low and are considerably inferior to those suggested as the acceptable minimum strength for clinical bonding[27,28], zinc phosphate cements have been successfully used in the clinics for a very long time to lute cast dental restorations. To assess the clinical performance of bonding systems, *in vitro* studies should therefore be supplemented with clinical studies with long follow-up times.

In most of the earlier studies dealing with zirconia specimens, various surface pretreatments – such as sandblasting or tribochemical silica coasting followed by silanization – were used[13-19]. However, mechanical treatments of zirconia should be done with caution because it has been demonstrated that heat treatment, sandblasting, and grinding can influence its mechanical properties[10,32,33]. In a recent study by Sundh and Sjögren, it was stated that the effect on the fracture resistance of zirconia depended on, among other things, the time the specimens were subjected to sandblasting[10]. This is probably because sandblasting treatment and/or grinding can induce compressive stresses and/or phase transformation on the surface, which increases the strength; at the same time, they also induce flaws and other defects which reduce the strength. Therefore, to find the best possible technique of improving bonding durability, more studies are needed to determine the effects of surface treatment on the bond strength and mechanical properties of zirconia ceramics.

CONCLUSIONS

Within the limitations of this *in vitro* study, the following conclusions were drawn:

1. Difference in surface roughness between SiC- and Al_2O_3-blasted specimens did not significantly affect bonding strength.
2. In all surface pretreatments, the shear bond strength significantly increased in the order of adhesive resin composite cement > glass ionomer cement > zinc phosphate cement.
3. The combination of adhesive resin composite cement with 10% methacryloxy propyl trimethoxysilane-toluene (dehydrated) solution yielded a slightly higher bond strength to YPSZ, as compared to the other surface treatment.

ACKNOWLEDGEMENTS

This study was supported by a Grant-in-aid for Scientific Research (B), No.18390509, from the Ministry of Education, Culture, Sports, Science and Technology, Japan.

REFERENCES

1) Green DJ, Hannink RHJ, Swain MV. Transformation toughening of ceramics, CRC Press, Boca Raton, 1989, pp.137-144.
2) Piconi C, Maccauro G. Zirconia as a ceramic biomaterial. Biomaterials 1999; 20: 1-25.
3) Cales B, Stefani Y, Lilley E. Long-term *in vivo* and *in vitro* aging of a zirconia ceramic used in orthopaedy. J Biomed Mater Res 1997; 28: 619-624.
4) Koutayas SO, Kern M. All-ceramic posts and cores: The state of the art. Quintessence Int 1999; 30: 383-392.
5) Akagawa Y, Ichikawa Y, Nikai H, Tsuru H. Interface histology of unloaded and early loaded partially stabilized zirconia endosseous implant in initial bone healing. J Prosthet Dent 1993; 69: 599-604.
6) Sjölin R, Sundh A, Bergman M. The Decim system for the production of dental restorations. Int J Computerized Dent 1999; 2: 197-207.
7) Filser F, Kocher P, Weibel F, Luthy H, Scharer P, Gauckler LJ. Reliability and strength of all-ceramic dental restorations fabricated by direct ceramic machining (DCM). Int J Comput Dent 2001; 4: 89-106.
8) Sundh A, Sjögren G. A comparison of fracture strength of yttrium-oxide-partially-stabilized zirconia ceramic crowns with varying core thickness, shapes and veneer ceramics. J Oral Rehabil 2004; 31: 682-688.
9) Sundh A, Molin M, Sjögren G. Fracture resistance of yttrium oxide partially-stabilized zirconia all-ceramic bridges after veneering and mechanical fatigue testing. Dent Mater 2005; 21: 476-482.
10) Sundh A, Sjögren G. Fracture resistance of all-ceramic zirconia bridges with differing phase stabilizers and quality of sintering. Dent Mater 2006; 22: 778-784.
11) Uo M, Sjögren G, Sundh A, Watari F, Bergman M, Lerner U. Cytotoxicity and bonding property of dental ceramics. Dent Mater 2003; 19: 487-492.
12) Kern M, Wegner SM. Bonding to zirconia ceramic: adhesion methods and their durability. Dent Mater 1998; 14: 64-71.
13) Blatz MB, Sadan A, Martin J, Lang B. *In vitro* evaluation of shear bond strengths of resin to densely-sintered high-purity zirconium-oxide ceramic after long-term storage and thermal cycling. J Prosthet Dent 2004; 91: 356-362.
14) Piwowarczyk A, Lauer HC, Sorensen JA. The shear bond strength between luting cements and zirconia ceramics after two pre-treatments. Oper Dent 2005; 30: 382-388.
15) Ernst CP, Cohnen U, Stender E, Willershausen B. *In vitro* retentive strength of zirconium oxide ceramic crowns using different luting agents. J Prosthet Dent 2005; 93: 551-558.
16) Derand T, Molin M, Kvam K. Bond strength of composite luting cement to zirconia ceramic surfaces. Dent Mater 2005; 21: 1158-1162.
17) Lüthy H, Loeffel O, Hammerle CH. Effect of thermocycling on bond strength of luting cements to zirconia ceramic. Dent Mater 2006; 22: 195-200.
18) Matinlinna JP, Heikkinen T, Ozcan M, Lassila LV, Vallittu PK. Evaluation of resin adhesion to zirconia ceramic using some organosilanes. Dent Mater 2006; 22: 824-831.
19) Wolfart M, Lehmann F, Wolfart S, Kern M. Durability of the resin bond strength to zirconia ceramic after using different surface conditioning methods. Dent Mater (in press).
20) Ernst CP, Cohnen U, Stender E, Willershausen B. *In vitro* retentive strength of zirconium oxide ceramic crowns using different luting agents. J Prosthet Dent 2005; 93: 551-558.
21) Aida, M, Hayakawa T, Mizukawa K. Adhesion of composite to porcelain with various surface conditions. J Prosthet Dent 1995; 73: 464-470.
22) Matsumura H, Kato H, Atsuta M. Shear bond strength to feldspathic porcelain of two luting cements in combination with three surface treatments. J Prosthet Dent 1997; 78: 511-517.
23) Kamada K, Yoshida K, Atsuta M. Effect of ceramic surface treatments on the bond of four resin luting agents to a ceramic material. J Prosthet Dent 1998; 79: 508-513.
24) Bayindir YZ, Bayindir F, Akyil SM. Bond strength of permanent cements in cementing cast to crown different core build-up materials. Dent Mater J 2004; 23: 117-120.
25) Ide T, Tanoue N, Yanagida H, Atsuta M, Matsumura H. Effectiveness of bonding systems on bonding durability of a prefabricated porcelain material. Dent Mater J 2005; 24: 257-260.
26) Wada T. Development of a new adhesive material and its properties. In: Proceedings of the International Symposium on Adhesive Prosthodontics, Amsterdam, Netherlands, Chicago: Academy of Dental Materials; 1986, p.9-18.
27) Kappert HF, Krah M. Keramiken-eine Übersicht. Quintessenz Zahntech 2001; 2: 668-704.
28) Thurmond J, Barkmeier W, Wildweding M. Effect of porcelain surface treatments on bond strength of composite resin bonded to porcelain. J Prosthet Dent 1994; 72: 355-359.
29) Piwowarczyk A, Bender R, Ottl P, Lauer HC. Long-term bond between dual-polymerizing cementing agents and human hard dental tissue. Dent Mater (in press).
30) Øilo G. Adhesive bonding of dental luting cements: influence of surface treatment. Acta Odontol Scand 1978; 36: 263-270.
31) Richardson DW, Tao L, Pashley DH. Bond strengths of luting cements to potassium oxalate-treated dentin. J Prosthet Dent 1990; 63: 418-422.
32) Zhang Y, Lawn BR, Rekow ED, Thompson VP. Effect of sandblasting on the long-term performance of dental ceramics. J Biomed Mater Res B Appl Biomater 2004; 15: 381-386.
33) Guazzato M, Quach L, Albakry M, Swain MV. Influence of surface and heat treatments on the flexural strength of Y-TZP dental ceramic. J Dent 2005; 33: 9-18.

Single-walled carbon nanotube-derived novel structural material

Go Yamamoto[a)]
Fracture and Reliability Research Institute, Tohoku University, Aramaki, Aoba-ku, Sendai 980-8579, Japan

Yoshinori Sato
Graduate School of Environmental Studies, Tohoku University, Aramaki, Aoba-ku, Sendai 980-857, Japan

Toru Takahashi, Mamoru Omori, and Toshiyuki Hashida
Fracture and Reliability Research Institute, Tohoku University, Aramaki, Aoba-ku, Sendai 980-8579, Japan

Akira Okubo
Institute of Materials Research, Tohoku University, Aoba-ku, Sendai 980-8577, Japan

Kazuyuki Tohji
Graduate School of Environmental Studies, Tohoku University, Aramaki, Aoba-ku, Sendai 980-857, Japan

(Received 22 October 2005; accepted 16 March 2006)

Binder-free macroscopic single-walled carbon nanotube (SWCNT) solids were prepared by spark plasma sintering (SPS) of purified SWCNTs. The effects of processing temperatures and pressures on the mechanical properties of the SWCNT solids and structural change of SWCNTs in the SWCNT solids were investigated. Transmission electron microscope observation of the SWCNT solids revealed that the high-temperature treatment has transformed some part of the SWCNTs into amorphous-like structure and the rest of the SWCNTs remained buried into the above structure. The mechanical properties of the SWCNT solids increased with the increasing processing temperature, probably reflecting the improvement of interfacial strength between SWCNTs and disordered structure of carbon due to the spark plasma generated in the SPS process.

I. INTRODUCTION

The predicted extraordinary mechanical, thermal, and electrical properties of single-walled carbon nanotubes (SWCNTs) have prompted intense research into a wide range of applications in structural materials, electronics, chemical processing, and energy management.[1] In particular, the exceptional mechanical properties of this material, along with the high aspect ratio, offer great potential and an alternative for traditional fibrous materials used as reinforcing components for ultrastrong composite materials. However, the production of SWCNT-reinforced composites with unprecedented mechanical properties is yet to be realized,[2–7] as the critical challenges lie in uniformly dispersing the SWCNTs in composites, achieving nanotube-matrix cohesion that provides effective stress transfer, and avoiding intra-bundle sliding within SWCNT bundles. In addition, we believe that, to take full advantage of the intrinsic physical and mechanical properties of SWCNTs, it is necessary to produce solid structures composed entirely of SWCNTs. Recently, a number of attempts to form such macroscopic products have been reported.[8–11] Sreekumar et al. produced SWCNT films composed entirely of SWCNTs and examined their mechanical properties by employing the tensile tests. The elastic modulus and fracture strength of the films with a density of 0.9 Mg/m^3 were 8 GPa and 30 MPa, respectively.[10] However, the strengthening mechanism for the observed mechanical properties and the contribution of the SWCNTs to the mechanical properties of the solid structures was not clearly established. In our previous study, we succeeded in preparing binder-free macroscopic SWCNT solids by using a spark plasma sintering (SPS) method and a hot-pressing method and investigated the mechanical properties and microstructures.[12] The SWCNT solids exhibited a nonlinear deformation response with elastic modulus of about 6.0 GPa and fracture strength of about 23.8 MPa.

a)Address all correspondence to this author.
e-mail: gyamamoto@rift.mech.tohoku.ac.jp
DOI: 10.1557/JMR.2006.0186

Transmission electron microscope (TEM) observation suggested that the failure occurred via intra-bundle sliding due to the weak cohesive bonds between SWCNTs within and between the bundles. A similar weak bond has been observed in macroscopic structures composed of SWCNTs.[2–7] As a consequence, a number of attempts to introduce stable links between SWCNTs have been recently reported.[13,14] Kis and co-workers successfully introduced stable links between neighboring SWCNTs within bundles, using moderate electron-beam irradiation inside a transmission electron microscope.[14] The irradiated bundles showed a substantial increase in elastic modulus. However, the electron-beam technique is impractical when it comes to the production of macroscopic solid structures. We believe that similar improvement of macrostructures can be realized by treating purified SWCNTs using SPS. The SPS technique is a pressure-assisted fast sintering method based on high-temperature plasma momentarily generated in the gaps between powder materials by electrical discharge during on–off direct current pulsing, which causes localized high temperatures. It has been suggested that the direct current pulse could generate several effects such as spark plasma, spark impact, Joule heating, and an electrical field diffusion.[15] These effects associated with the SPS technique may be helpful in formin stable links between SWCNTs within and between the bundles, and an enhancement in the mechanical properties of binder-free SWCNT solids may be expected. In this investigation, the effects of processing temperatures and pressures on the mechanical properties of the SWCNT solids prepared by the SPS method and structural change of SWCNTs in the SWCNT solids were further investigated, based on our previous study.[12]

II. EXPERIMENTAL

The preparation of the highly pure SWCNTs was carried out using a technique described elsewhere.[12,16] The purified SWCNTs used in this study were prepared by subjecting the soot synthesized by an arc discharge method to heat treatment under an oxidizing atmosphere and chemical treatment in hydrochloric acid. The diameter and bundle length of purified SWCNTs estimated from Raman scattering measurements[17] and scanning electron microscopy (SEM) ranged between 1.33 and 1.52 nm and 1.5 and 22.0 μm, respectively.

The binder-free SWCNT solids were prepared by sintering the purified SWCNTs at temperatures of 1000, 1200, and 1400 °C under a pressure of 120 MPa in vacuum for 5 min in a 20-mm-diameter graphite die. The binder-free SWCNT solids prepared in this study are demonstrated in Fig. 1. The disk-shaped specimen measuring 20 mm in diameter and 1.5 mm in thickness was cut using a silicon carbide saw and polished into 2 × 1 × 18 mm pieces. The mechanical properties of the solids, the elastic modulus, and the fracture strength were determined by the three-point bending tests, which were performed on a universal testing machine (Instron 5582, Instron Corporation, Norwood, MA) in atmospheric conditions at room temperature. The application of load was performed at a crosshead speed of 0.05 mm/min. The elastic modulus E_b and fracture strength σ_b were determined from load versus load-line displacement records using the simple beam theory. The initial slope of the load versus load-line displacement curves was used to compute the elastic modulus. For each processing condition, three specimens were tested, and the averaged results are presented below.

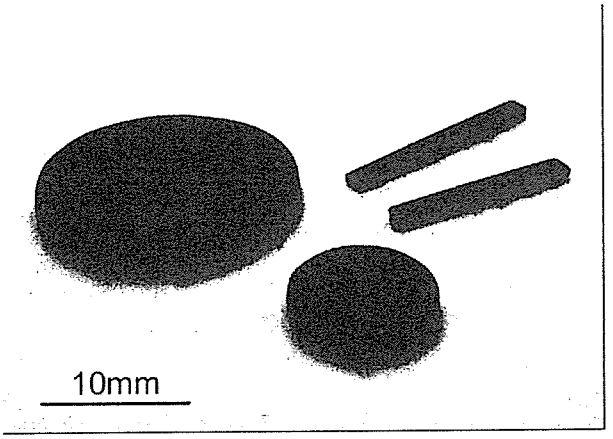

FIG. 1. Binder-free SWCNTs solids prepared by SPS; two disk-shaped specimens have diameters of 10 and 20 mm and thickness of about 1.5 mm.

III. RESULTS AND DISCUSSION

Typical TEM (Hitachi HF-2000, Tokyo, Japan) images of the fracture surfaces are shown in Figs. 2(a) and 2(b) for the solids prepared at 1000 and 1400 °C, respectively. The TEM image of the solid prepared at 1000 °C shows numerous smooth surfaced bundles [Fig. 2(a)]. However in the case of 1400 °C, the number of SWCNT bundles present was found to be lesser, and at the same time the presence of disordered structure of carbon was also observed. Detailed TEM observation suggested that the high-temperature treatment transformed some part of the SWCNTs into disordered structure of carbon, and the rest of the SWCNTs remained buried into the above structure [Fig. 2(b)]. Because of their metastable character, SWCNTs may transform into more stable structure under the high-temperature conditions.

Thus, we used Raman spectroscopy (Jobin-Yvon T64000, Kyoto, Japan) and x-ray diffractometry (XRD; Mac Science M21X, Ibaragi, Japan) to analyze the disordered structure of carbon present in the solids. In the Raman analysis, it is well known that the ratio of the

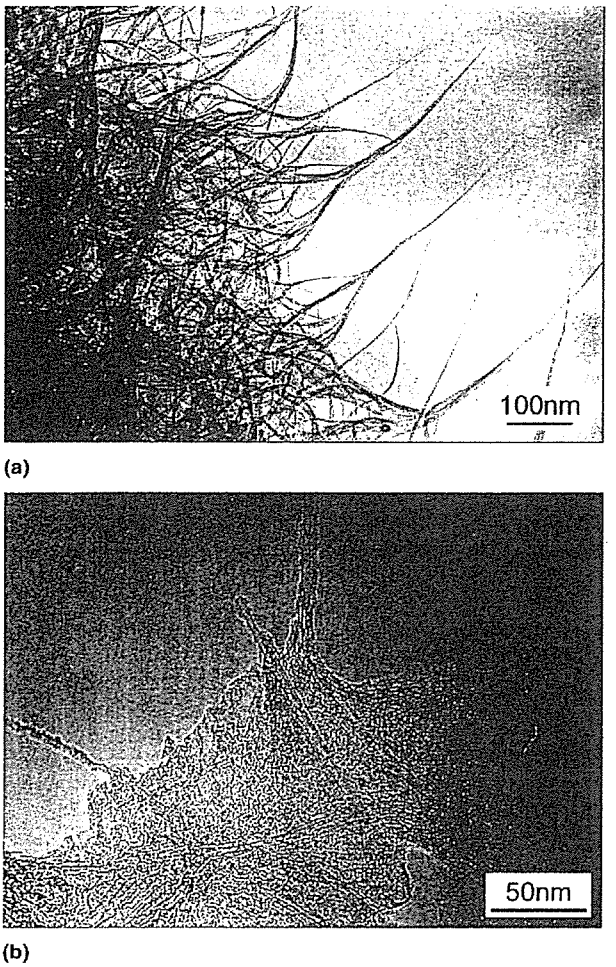

FIG. 2. Typical TEM images of the fracture surfaces for the SWCNT solids prepared by SPS at temperatures of (a) 1000 °C and (b) 1400 °C.

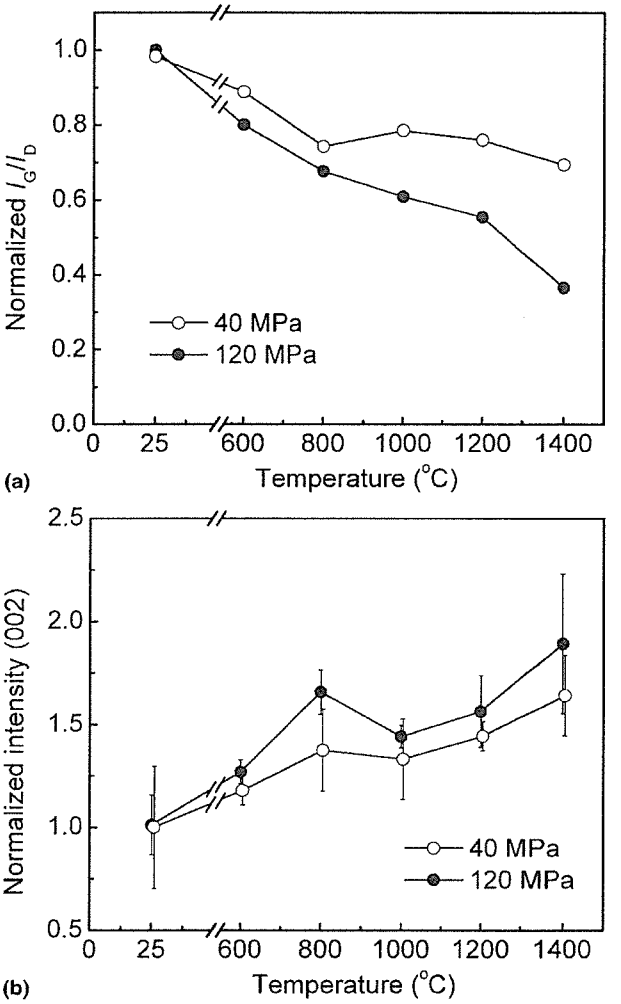

FIG. 3. (a) Raman intensity ratio I_G/I_D and (b) normalized intensity (002) for the SWCNT solids prepared by SPS under various processing conditions.

peak intensities at about 1350 cm^{-1} (D-band, I_D) and 1590 cm^{-1} (G-band, I_G) is a good index to evaluate the abundance of SWCNTs in the sample.[18,19] Thus, we prepared SWCNT solids under pressures of 40 and 120 MPa by using mechanical compaction at room temperature and SPS at temperatures between 600 and 1400 °C. Figure 3(a) shows Raman intensity ratio (I_G/I_D) for the solids prepared under various processing conditions. Here, the I_G/I_D was normalized using the results of solids consolidated by mechanical compaction under a pressure of 120 MPa. It should be mentioned here that the general feature of the Raman profile obtained in this study is very similar to that observed for the SWCNTs, as purified. The Raman and XRD profiles of the SWCNTs purified using the same method as that of this study have been reported in our previous study.[16] The reader is referred to the literature for the Raman and XRD profiles of the purified SWCNTs. As shown in Fig. 3(a), the I_G/I_D of solids prepared by mechanical compaction at room temperature was independent of the applied pressure. However, in the case of the solids prepared by SPS, the I_G/I_D gradually decreased with increasing temperature and pressure, suggesting the transformation of SWCNTs in the solids. This is may be attributable to an increase in defect concentration on the SWCNTs structure caused during the SPS process, which may lead to the formation of disordered structure of carbon in stringent conditions. However, the Raman analysis provides no information about the structure of the solids prepared by SPS. Thus, we also carried out the XRD analysis of the solids prepared under the various conditions.

The XRD profiles exhibited the peaks corresponding to the reflections from (002) and (004) planes of graphite in all the solids. Figure 3(b) shows normalized value of the (002) reflection obtained from the XRD patterns for the solids. Here, the measurements were normalized

using the results of solids consolidated by mechanical compaction under a pressure of 40 MPa. The intensity for the solids prepared by mechanical compaction at room temperature was independent of the applied pressure, just like data obtained from the Raman analysis. However, in the case of the solids prepared by SPS, the intensity increased steadily with the increase in processing temperatures and pressures. The above XRD results, in conjunction with the TEM and Raman data, suggest that the SWCNTs were transformed into graphite-like and amorphous-like structures during the SPS process. Additional evidence for the structural changes in the SWCNT solids may be gained from further examination of the XRD result. The XRD results on the SWCNT solids were analyzed using the experimental data in the low-frequency regions (scanning angle of 2θ was 5–26°), referring to the literature.[20] Plotting the XRD intensity against scattering vector Q revealed that a well-defined peak existed at Q = 0.42 Å, and weaker peaks, up to 1.8 Å. These low-frequency scattering peaks indicate the existence of a two-dimensional lattice of SWCNTs organized in bundles.[20] The average transverse size of the SWCNT bundles, which was calculated from a full width at half-maximum (FWHM) of the peak at Q = 0.42 Å, decreased with the increasing processing temperatures and pressures. At the same time, the intensity of the peak at Q = 0.42 Å decreased with the increasing processing temperatures and pressures. These results may also support the transformation of the SWCNTs in the SPS process. The rise in the concentration of the graphite-like and amorphous-like materials in the solids may lead to the change in their physical and mechanical properties.

The theoretical density of individual SWCNTs has been calculated to be 1.36 Mg/m^3, assuming the diameter of the SWCNTs to be 1.3 nm, and the distance between neighboring SWCNTs is determined by the van der Waals interaction.[21] The measurements of the solids consolidated by mechanical compaction under a pressure of 120 MPa was 1.04 Mg/m^3. On the other hand, the densities of the solids prepared by using SPS have been found to be larger than the ones prepared by mechanical compaction. The measurement of the solids prepared at 600 °C was 1.35 Mg/m^3 and almost equal to the theoretical density, and the value of the solids prepared at 1400 °C was 1.46 Mg/m^3. In general, true density of porous solids, such as pycnometry data, provides higher value than bulk density. Thus, the bulk density data described above suggest that the rise in the density of the solids with treatment temperature may be due to the structural change of SWCNTs into the graphite-like and amorphous-like structures.

Figure 4 gives typical load versus load-line displacement curves of the solids determined by three-point bending tests. In all the specimens, a nonlinear deformation response was observed up to the peak load, and a relatively rapid crack extension took place just after the peak load followed by a long tail. Therefore, the SWCNT solids may be categorized as a quasi-brittle material. The deformation response of macroscopic structures composed of SWCNTs have exhibited brittle nature,[5,7,10] although post-peak behavior is observed for binder-free SWCNT solids. This type of unusual deformation response was believed due to the presence of bundle structures. The processing conditions and the mechanical properties of the solids determined by the three-point bending tests are summarized in Table I. Mechanical measurements revealed that the mechanical properties of the solids were dependent on the processing temperature. The reason for the improvement of the mechanical properties may be due to the effective prevention of slide deformation between the bundles, through the formation of stable links between SWCNTs. However, the mechanical properties of the solids are inferior than those of individual SWCNTs.[22,23]

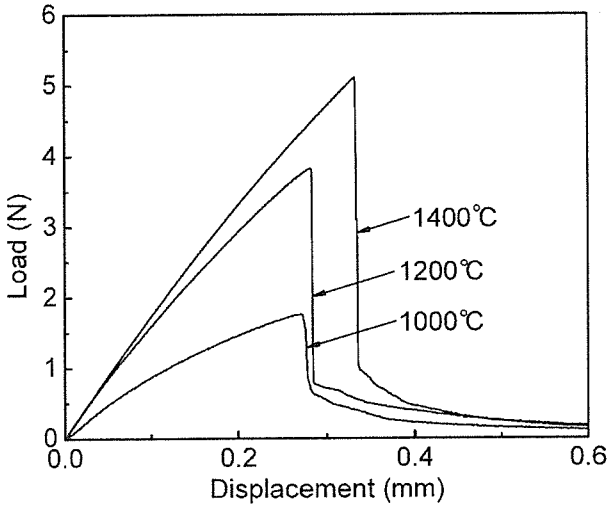

FIG. 4. Typical load versus load-line displacement curves of the SWCNT solids, which show the quasi-brittle nature.

We now discuss the correspondence between the mechanical property and microstructure of the SWCNT solids using TEM observation, shown in Figs. 2(a) and 2(b). From the fracture surface of the solids prepared at 1000 °C, the following features can be noted. First, numerous bundles protruded from the fracture surface. The

TABLE I. Processing conditions and mechanical properties for the SWCNT solids prepared by spark plasma sintering.

Processing conditions	Elastic modulus E_b (GPa)	Fracture strength σ_b (MPa)
1000 °C, 120 MPa	6.04	23.8
1200 °C, 120 MPa	7.06	50.1
1400 °C, 120 MPa	8.30	52.4

diameter of "pullout" bundles gradually decreased toward their tip, which was generally about 3 μm long, and in some cases it was 8 μm or longer. In addition, numerous curved and stretched SWCNT bundles that bridged the 3-μm-wide cracks were observed through the SEM data. This curving and stretching reflected the high flexibility of the SWCNT bundles, which may be the cause of the post-peak behavior observed in Fig. 4. The bundles may have been pulled out during the deformation and fracture of the solids. Second, TEM observations showed that the pulled out bundles consisted of about 10–30 nanotubes, and no breakage of SWCNTs in the bundles was observed. These observations revealed that the failure occurred via inter-bundles slippage rather than the failure of the SWCNTs themselves, suggesting that the detachment between SWCNTs within and between the bundles is a very decisive factor in the fracture process of the solids. However, when the processing temperature was further increased, the pulled out region was observed to decrease. As seen in Fig. 2(b), only a limited extent of pullout is observed in the solid prepared at 1400 °C. The pullout length of the bundles was obviously shorter, and the number of SWCNT bundles present was less than that of the solids prepared at 1000 °C. It is noted that SWCNT bundles are embedded in the amorphous-like structure, which is transformed from SWCNTs. The tighter links between the SWCNTs and amorphous-like structure may cause the improved mechanical properties that occur when the materials are prepared at higher processing temperatures.

IV. CONCLUSIONS

In summary, we have demonstrated the preparation of binder-free SWCNT solids with elastic modulus and fracture strength of 8.3 GPa and 52.4 MPa, respectively, by using the SPS technique. The experimental observation revealed that the high-temperature treatment transformed some part of the SWCNTs into amorphous-like structure, and the rest of the SWCNTs remained buried in that structure. The mechanical properties of the SWCNT solids increased with increasing processing temperature, probably reflecting the improvement of interfacial strength between SWCNTs and amorphous-like structure transformed from SWCNTs caused by the spark plasma generated in the SPS process. The results of this study may open up a new route for the large-scale production of binder-free macroscopic SWCNT solid structures. Further research is currently underway to examine the influence of nanotube types, purity, and anisotropy on the mechanical and electrical properties binder-free SWCNT solids. The binder-free SWCNT solids could also be applied to biomaterials such as artificial heart valves and tooth roots.[24]

ACKNOWLEDGMENTS

This work was supported by the Japan Ministry of Health, Labor and Welfare under Grants-in-Aid for Research on Advanced Medical Technology and by the 21st Century Center of Excellence (COE) Program Grant of the International COE of Flow Dynamics, Ministry of Education, Culture, Sports, Science and Technology. The authors thank Mr. K. Motomiya of Graduate School of Engineering, Tohoku University for his technical assistance in TEM analysis. G.Y. thanks Prof. B. Jeyadevan of Graduate School of Environmental Studies, Tohoku University for useful discussion.

REFERENCES

1. R.H. Baughman, A.A. Zakhidov, and W.A. de Heer: Carbon nanotubes—the route toward applications. *Science* **297**, 787 (2002).
2. R.Z. Ma, J. Wu, B.Q. Wei, J. Liang, and D.H. Wu: Processing and properties of carbon nanotubes-nano-SiC ceramic. *J. Mater. Sci.* **33**, 5243 (1998).
3. P.M. Ajayan, L.S. Schadler, C. Giannaris, and A. Rudio: Single-walled carbon nanotube-polymer composites: Strength and weakness. *Adv. Mater.* **12**, 750 (2000).
4. E. Flahaut, A. Peigney, Ch. Laurent, Ch. Marliere, F. Chastel, and A. Rousset: Carbon nanotube-metal-oxide nanocomposites: Microstructure, electrical conductivity and mechanical properties. *Acta Mater.* **48**, 3803 (2000).
5. B. Vigolo, A. Penicaud, C. Coulon, C. Sauder, R. Pailler, C. Journet, P. Bernier, and P. Poulin: Macroscopic fibers and ribbons of oriented carbon nanotubes. *Science* **290**, 1331 (2000).
6. G-D. Zhan, J.D. Kuntz, J. Wan, and A.K. Mukherjee: Single-walled carbon nanotubes as attractive toughening agents in alumina-based nanocomposites. *Nat. Mater.* **2**, 38 (2003).
7. B.G. Min, T.V. Sreekumar, T. Uchida, and S. Kumar: Oxidative stabilization of PAN/SWNT composite fiber. *Carbon* **43**, 599 (2005).
8. R.Z. Ma, C.L. Xu, B.Q. Wei, J. Liang, D.H. Wu, and D.J. Li: Electrical conductivity and field-emission characteristics of hot-pressed sintered carbon nanotubes. *Mater. Res. Bull.* **34**, 741 (1999).
9. Y-H. Li, C. Xu, B. Wei, X. Zhang, M. Zhang, D. Wu, and P.M. Ajayan: Self-organized ribbons of aligned carbon nanotubes. *Chem. Mater.* **14**, 483 (2002).
10. T.V. Sreekumar, T. Liu, and S. Kumar: Single-wall carbon nanotube films. *Chem. Mater.* **15**, 175 (2003).
11. L.S. Ericson, L.M. Ericson, H. Fan, H. Peng, V.A. Davis, W. Zhou, J. Sulpizio, Y. Wang, R. Booker, J. Vavro, C. Guthy, A.N.G. Parra-Vasquez, M.J. Kim, S. Ramesh, R.K. Saini, C. Kittrell, G. Lavin, H. Schmidt, W.W. Adams, W.E. Billups, M. Pasquali, W-F. Hwang, R.H. Hauge, J.E. Fischer, and R.E. Smalley: Macroscopic, neat, single-walled carbon nanotube fibers. *Science* **305**, 1447 (2004).
12. G. Yamamoto, Y. Sato, T. Takahashi, M. Omori, T. Hashida, A. Okubo, S. Watanabe, and K. Tohji: Preparation of single-walled carbon nanotube solids and their mechanical properties. *J. Mater. Res.* **20**, 2609 (2005).
13. M. Terrones, H. Terrones, F. Banhart, J-C. Charlier, and P.M. Ajayan: Coalescence of single-walled carbon nanotubes. *Science* **288**, 1226 (2000).
14. A. Kis, G. Csanyi, J-P. Salvetat, T-N. Lee, E. Couteau, A.J. Kulik,

W. Benoit, J. Brugger, and L. Forro: Reinforcement of single-walled carbon nanotube bundles by intertube bridging. *Nat. Mater.* **3,** 153 (2004).
15. M. Omori: Sintering, consolidation, reaction and crystal growth by the spark plasma system (SPS). *Mater. Sci. Eng. A* **287,** 183 (2000).
16. G. Yamamoto, Y. Sato, T. Takahashi, M. Omori, A. Okubo, K. Tohji, and T. Hashida: Mechanical properties of binder-free single-walled carbon nanotube solids. *Scripta Mater.* **54,** 299 (2006).
17. S.M. Bachilo, M.S. Strano, C. Kittrell, R.H. Hauge, R.E. Smalley, and R.B. Weisman: Structure-assigned optical spectra of single-walled carbon nanotubes. *Science* **298,** 2361 (2002).
18. H. Kataura, Y. Kumazawa, Y. Maniwa, Y. Ohtsuka, R. Sen, S. Suzuki, and Y. Achiba: Diameter control of single-walled carbon nanotubes. *Carbon* **38,** 1691 (2000).
19. Y. Sato, B. Jeyadevan, R. Hatakeyama, A. Kasuya, and K. Tohji: Electronic properties of radial single-walled carbon nanotubes. *Chem. Phys. Lett.* **385,** 323 (2004).
20. A. Thess, R. Lee, P. Nikolaev, H. Dai, P. Petit, J. Robert, C. Xu, Y.H. Lee, S.G. Kim, A.G. Rinzler, D.T. Colbert, G.E. Scuseria, D. Tomanek, J.E. Fischer, and R.E. Smalley: Crystalline ropes of metallic carbon nanotubes. *Science* **273,** 483 (1996).
21. Y. Saito and S. Bandou: *Introduction to Carbon Nanotubes* (Corona Publishing, Tokyo, Japan, 1998), p. 35.
22. F. Li, H.M. Cheng, S. Bai, and G. Su: Tensile strength of single-walled carbon nanotubes directly measured from their macroscopic ropes. *Appl. Phys. Lett.* **77,** 3161 (2000).
23. M-F. Yu, B.S. Files, S. Arepalli, and R.S. Ruoff: Tensile loading of ropes of single wall carbon nanotubes and their mechanical properties. *Phys. Rev. Lett.* **84,** 5552 (2000).
24. Y. Sato, M. Ohtsubo, B. Jeyadevan, K. Tohji, K. Motomiya, R. Hatakeyama, G. Yamamoto, M. Omori, T. Hashida, K. Tamura, T. Akasaka, M. Uo, A. Yokoyama, and F. Watari: Biocompatibility of carbon nanotube disk, in *Proceedings of SPIE*, Vol. 5593, edited by M.S. Islam and A.K. Dutta (SPIE, Bellingham, WA, 2004), p. 623.

Available online at www.sciencedirect.com
SCIENCE DIRECT®
Scripta Materialia 54 (2006) 299–303
Scripta MATERIALIA
www.actamat-journals.com

Mechanical properties of binder-free single-walled carbon nanotube solids

Go Yamamoto [a,*], Yoshinori Sato [b], Toru Takahashi [a], Mamoru Omori [a], Akira Okubo [c], Kazuyuki Tohji [b], Toshiyuki Hashida [a]

[a] *Fracture and Reliability Research Institute, Tohoku University, Graduate School of Engineering, 6-6-1 Aza-Aoba, Aramaki, Aobaku, Sendai, Miyagi 980-8579, Japan*
[b] *Graduate School of Environmental Studies, Tohoku University, Sendai 980-8579, Japan*
[c] *Institute for Materials Research, Tohoku University, Sendai 980-8577, Japan*

Received 9 January 2005; received in revised form 8 March 2005; accepted 29 March 2005
Available online 25 October 2005

Abstract

Single-walled carbon nanotubes (SWCNTs) were successfully solidified without any additives using a spark plasma method. Purification of raw soot was crucially important in order to improve the mechanical properties of the SWCNT solid, which exhibited a significant nonlinear deformation response in contrast with brittle fracture of an unpurified SWCNT solid.

Keywords: Single-walled carbon nanotubes; Spark plasma sintering method; Small punch testing method; Mechanical properties; Microstructure

Recent experimental studies have amply demonstrated that individual single-walled carbon nanotubes (SWCNTs) have an extremely high Young's modulus and tensile strength [1,2]. Researchers have mostly examined the possible applications of SWCNTs in polymer [2,3], metal [4] and ceramics [5,6] matrices, and characterized the properties and microstructures of these composite materials. However, the production of SWCNT composites with extremely good mechanical properties is yet to be realized. Additionally, in order to take full advantage of the intrinsic mechanical and physical properties of SWCNTs, it is necessary to produce solid structures that are composed solely of the SWCNTs.

In this work, we have successfully produced binder-free SWCNT disks with purified SWCNTs by using a spark plasma sintering (SPS) method, and the mechanical properties of the disk specimens were investigated by a small punch (SP) testing method. Raw soot synthesized by conventional methods commonly contains metal particles and various forms of carbon [7–9]. Therefore, the effect of the impurities on the mechanical properties and microstructures was investigated by comparing the results obtained from the disk specimens made of the purified SWCNTs and unpurified raw soot.

SWCNTs were synthesized by a direct current arc discharge between a pure graphite cathode and a metal loaded graphite anode. A pure graphite rod (purity 99.9%), 16 mm diameter and 50 mm length, and a 6 mm diameter and 110 mm length graphite rod (99.9%) loaded with Fe and Ni powders (99.99%) were used as cathode and anode, respectively. The arc discharge was carried out under a helium atmosphere of 100 Torr. The discharge current was 70 A, and during the discharge, the gap between the electrodes was maintained at about 3 mm by manually advancing the consumed anode. The raw soot containing SWCNTs

* Corresponding author. Tel.: +81 22 217 7524; fax: +81 22 217 4311.
E-mail address: gyamamoto@rift.mech.tohoku.ac.jp (G. Yamamoto).

1359-6462/$ - see front matter © 2005 Acta Materialia Inc. Published by Elsevier Ltd. All rights reserved.
doi:10.1016/j.scriptamat.2005.03.053

produced by the arc discharge method was retrieved from the upper wall and the roof of the chamber and was homogenized by mixing together regardless of the different sampling locations. In the raw soot, SWCNTs coexist with many by-products such as metal particles, fullerenes, and amorphous carbon [7,10]. Therefore, SWCNTs were separated step by step from the impurities using the following purification process. First, the fullerenes and the amorphous carbon were burned out by heating approximately 600 mg of raw soot at 450 °C and keeping for 30 min in air. Then, the residual soot was heated up to 500 °C and kept for 30 min in air to burn out the graphitic layers surrounding metal particles. Finally, the metal particles were washed out from the soot by treating with 6 M hydrochloric acid solution. The processed soot was filtered and rinsed with deionized water.

Fig. 1(a) and (b) shows the Raman spectra and X-ray diffraction (XRD) profiles of the unpurified raw soot and purified SWCNTs, respectively. Abundance of SWCNTs in the sample is estimated from the intensity ratio I_G/I_D of the Raman spectrum, and is also indicated in Fig. 1(a). It is well known that the Raman intensity ratio I_G/I_D of the peaks at 1350 cm^{-1} (D-band) and 1590 cm^{-1} (G-band) is a good index for the evaluation of the SWCNTs abundance [11,12]. Here, both the samples were measured using 488.0 nm exciting lasers with backscattering configuration. As seen in Fig. 1(a), the I_G/I_D of SWCNTs was about seven times larger than that of raw soot, without any change in each peak position. The XRD profile of the raw soot shows the presence of the C_{60}, graphite and metals. In contrast, the SWCNTs were free of C_{60} and metals, showing only the graphite peak. These results suggest that highly pure SWCNTs have been obtained by the processing conditions used, except for a trace amount of carbon materials other than SWCNTs. The diameter distribution of SWCNTs was determined from the Raman spectra in radial breathing mode (RBM) range [13]. From the peaks at 160 and 180 cm^{-1}, the diameter of the SWCNTs was estimated to be approximately 1.52 and 1.33 nm. This result agrees with the diameter observed by TEM.

Purified SWCNTs and unpurified raw soot were solidified by using the SPS technique [14] in a graphite die with a diameter of 10 mm at a temperature of 1000 °C under a pressure of 120 MPa. After applying the given pressure, the samples were heated to the desired temperature and held at this temperature for 5 min. The prepared specimens were disk-shaped about 10 mm in diameter and 1.5 mm in thickness, and were then polished with emery paper (#4000) into 10 mm diameter and 1.2 mm thickness. The mechanical properties such as Young's modulus and work of fracture were measured by the SP testing method [15] using miniaturized disk specimens. The SP tests were performed on a

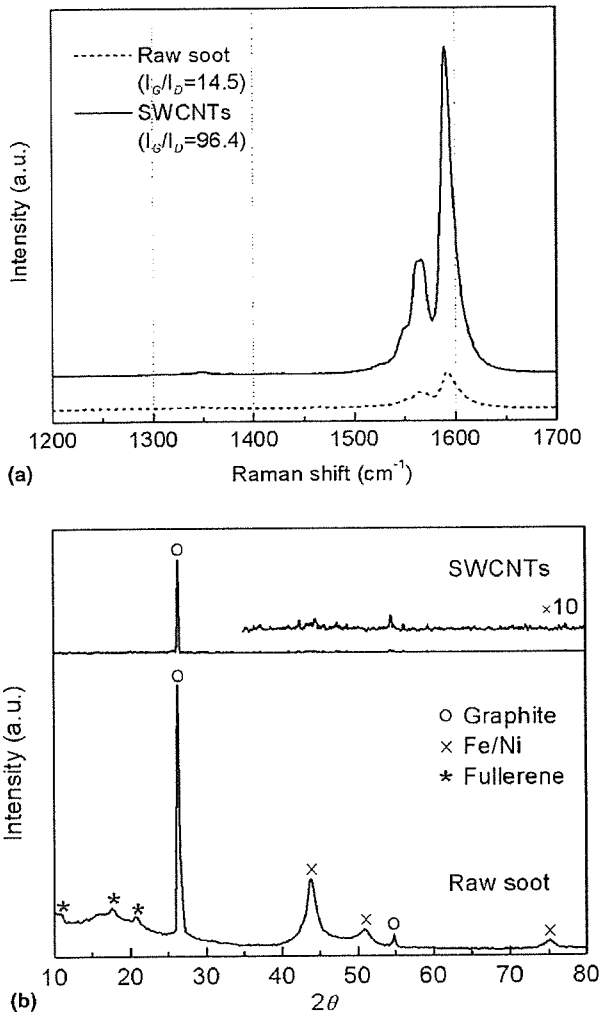

Fig. 1. (a) Raman spectra and (b) X-ray diffraction patterns of the unpurified raw soot and purified SWCNTs, respectively. The Raman intensity ratios I_G/I_D estimated from the peak position of the D-band and G-band are also indicated (a).

universal testing machine in atmospheric conditions at room temperature. The disk specimens were placed on a die having a central borehole and simply supported on the circular edge (see Ref. [15]). The load was applied at the specimen center through a puncher at a crosshead speed of 0.05 mm/min. The displacement of the specimens was monitored at the mid-point using a linear variable differential transducer (LVDT) fixed on to the testing machine.

Deformation and stress analysis for SP tests have been performed using a finite element method (FEM), assuming liner elastic response of the material [15]. In this study, the numerical data were used to compute Young's modulus and to construct a stress–normalized displacement diagram. The Young modulus of SP specimen E_{SP} was calculated from the measured initial linear slope of the load–displacement curve, which was expressed by the following equation:

$$E_{SP} = f(t/a)\frac{3a^2P(1-\nu)(3+\nu)}{4\delta\pi t^3} = f(t/a)\frac{P}{\delta}C_0, \quad (1)$$

where P is the load, δ the displacement measured at the specimen center, $f(t/a)$ the correction factor for the specimen thickness, a the borehole diameter of the supporting die (=2.1 mm), ν the Poisson's ratio, and t the specimen thickness. The maximum tensile stress along the load application point σ_{SP} can be expressed by the equation given below.

$$\sigma_{SP} = \frac{P}{t^2}(1+\nu)\left[0.485\ln\frac{a}{t} + 0.52 + \frac{3}{2\pi(1+\nu)}\right] = \frac{S_0}{t^2}P. \quad (2)$$

Eqs. (1) and (2) suggest that plotting the stress versus normalized displacement curve ($\sigma_{SP} - [S_0/f(t/a)C_0t]\delta$) provides an initial slope of Young's modulus E_{SP}. The work of fracture was calculated using the area of the stress–normalized displacement curve up to the maximum load. The disk specimens made of purified SWCNTs and unpurified raw soot are referred to as SWCNT disk and raw soot disk, respectively. For each processing condition, three specimens were tested and the averaged results will be presented below.

Figs. 2 and 3 show, respectively, the fractured specimens and typical stress–normalized displacement curves for both specimens. In the case of the raw soot disks, the main crack was formed at the center of the specimen that was subjected to the maximum biaxial stress and propagated to the outer region as shown in Fig. 2(a). The specimen was broken into four pieces, which demonstrated the brittle nature of the fracture. This observation corresponds to the deformation response as shown in Fig. 3. In contrast, the purified SWCNTs produced quasi-ductile solid structures. A fractured specimen is shown in Fig. 2(b), which is also illustrated schematically in Fig. 2(c). As shown in Fig. 2(c), an indentation was formed on the specimen by the spherical puncher used for load application, and the main fracture initiated and propagated from a cone-shaped region at the edge of the indentation. A significant non-linear deformation response was observed for the SWCNT disks, as shown in Fig. 3.

The physical and mechanical properties for both specimens are shown in Table 1. The bulk density of

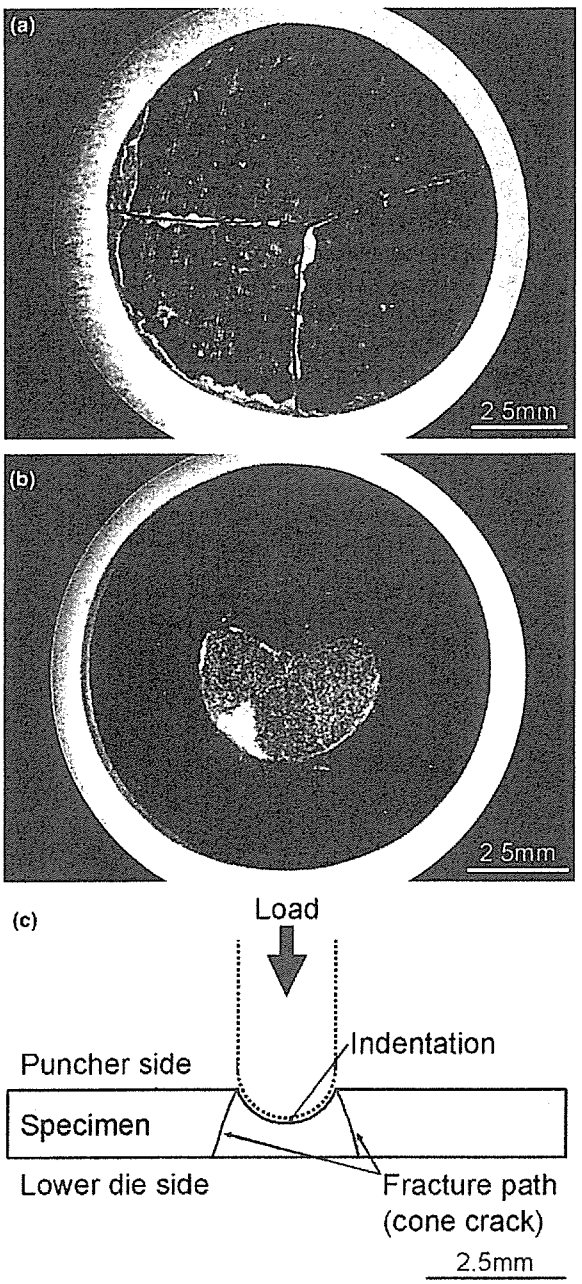

Fig. 2. Crack propagation of (a) the raw soot disk and (b) the SWCNT disk. (c) Schematic illustration of the fracture path is also shown.

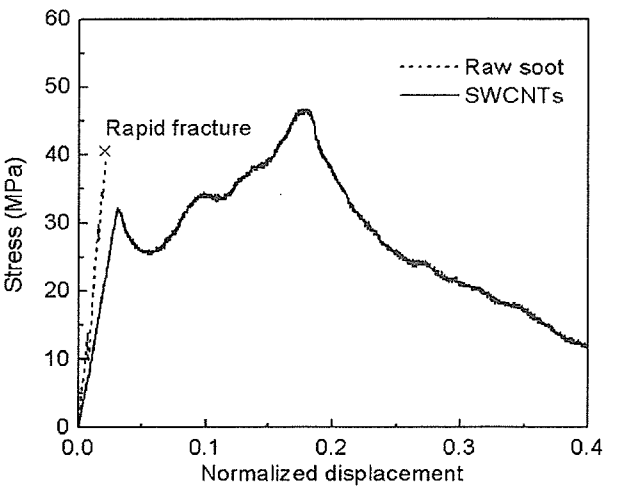

Fig. 3. Typical stress versus normalized displacement curves obtained from small punch tests. Dotted line and dark line show the fracture behavior of the raw soot disk and SWCNT disk, respectively.

Table 1
Physical and mechanical properties of the raw soot disks and SWCNT disks prepared by spark plasma sintering

Materials	Bulk density ρ (Mg/m^3)	Young's modulus E_{SP} (GPa)	Work of fracture J_{SP} (N mm)
Raw soot	1.90	0.74	1.4
SWCNTs	1.55	0.66	17.3

the raw soot disks was found to be larger than that of the SWCNT disks. This may be due to the presence of by-products such as metal particles, fullerenes and carbon materials in the raw soot disks. However, there was almost no difference in Young's modulus between the specimens. On the other hand, the work of fracture of the SWCNT disks was 12 times larger than that of the raw soot disks. The reason for the significant difference in the work of fracture may be due to the quasi-ductile fracture behavior of the SWCNT disks.

To obtain an in-depth understanding of the differences in the fracture mechanisms, the microstructural observation was carried out using a transmission electron microscope (TEM). Fig. 4 shows the typical low magnification TEM photographs of the fracture surfaces of (a) the raw soot disk and (b) the SWCNT disk. The raw soot disk consists of SWCNTs bundles (arrow A), amorphous carbon (arrow B) and metal particles (arrow C), as shown in Fig. 4(a). From the morphology of the fracture surface, it looks as if the SWCNT bundles have been pulled out from the body during the deformation and fracture of the specimen. Then, most pulled out bundles are curved and looped. However, it can be seen that the main material of fracture surface was entirely different from the structure of SWCNT bundles and the pullout was limited. In contrast, in the case of the SWCNT disk, extensive pullout of SWCNT bundles of approximately 1 μm in length were observed, and the diameter of SWCNT bundles was observed to decrease toward their tips. Fig. 4(c) is a high-resolution TEM photograph of the fracture surface of SWCNT disk. From the TEM photograph, it can be seen that numerous bundles containing 10–30 nanotubes protrude from the fracture surface, and the average diameter of SWCNTs in the bundles was 1.58 and 1.39 nm, which is in approximate agreement with the diameter of SWCNTs before the solidification process. Detailed observation of the fracture surface indicates that no breakage of SWCNTs occurred in the bundles for both cases. These experimental results indicate that the brittleness of the raw soot disks may be due to the inherent brittleness of carbon materials such as amorphous carbon and graphite, which possess no effective stress transfer capability between the bundles and

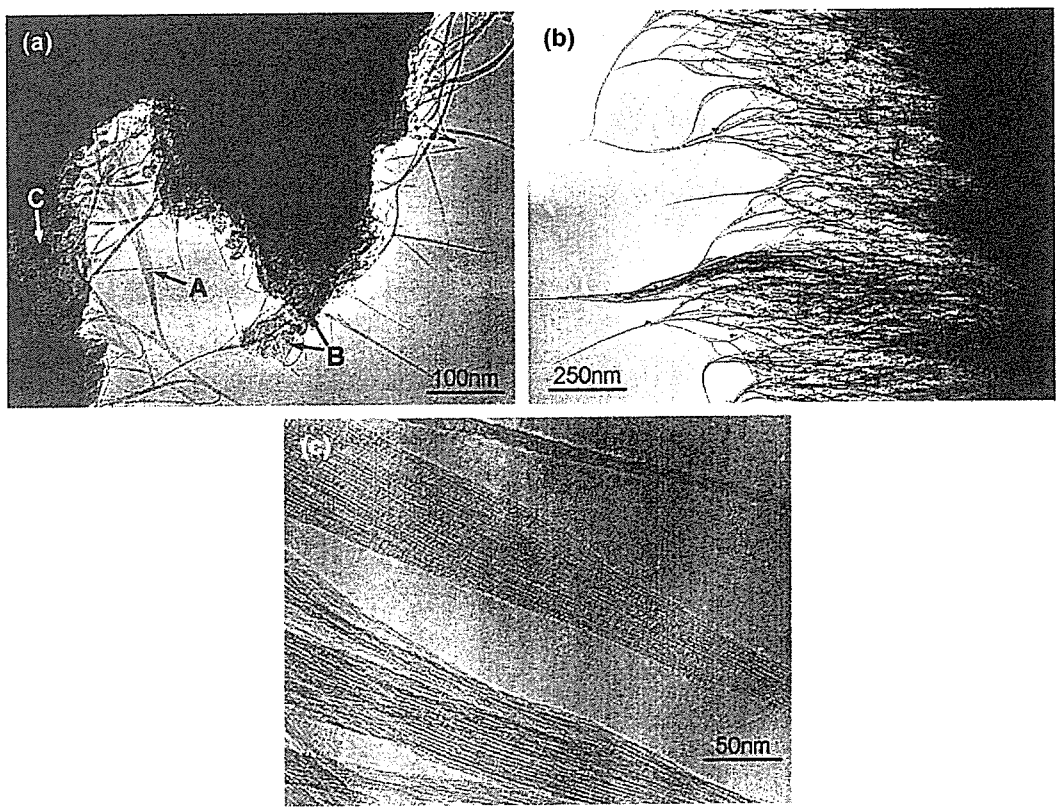

Fig. 4. Typical low magnification TEM photographs of fracture surfaces of (a) the raw soot disk and (b) the SWCNT disk. (c) A high-resolution TEM photograph of fracture surfaces of SWCNT disk.

carbon materials. In contrast, the failure in the SWCNT disks occurred via intra-bundle sliding between SWCNTs, within and between the bundles. The significant non-linear deformation response of the SWCNT disks may be due to the pullout behavior associated with the slippage of SWCNTs held by weak van der Waals interactions.

In this study, we have successfully produced SWCNT disks without any additives, employing the SPS method. This solidification method enables us to produce quasi-ductile solid structures composed of purified SWCNTs with Young's modulus of 0.66 GPa. In contrast, unpurified raw soot produced brittle solids structures with Young's modulus of 0.74 GPa. However, Young's modulus of the purified SWCNT disks is still lower than the individual SWCNTs due to the sliding of SWCNTs within the bundles. Work is in progress to improve the mechanical properties of the binder-free purified SWCNT disks by introducing effective chemical bonding between SWCNTs, within and between the bundles.

Acknowledgments

This work was supported by the Japan Ministry of Health, Labor and Welfare under Grants-in-Aid for Research on Advanced Medical Technology and the 21st Century COE Program Grant of the International COE of Flow Dynamics, which were supported by Ministry of Education, Culture, Sports, Science and Technology. We thank the staff at the Laboratory for Advanced Material of the Tohoku University for their assistance.

References

[1] Yu MF, Files BS, Arepalli S, Ruoff RS. Phys Rev Lett 2000;84:5552.
[2] Li F, Cheng HM, Bai S, Su G. Appl Phys Lett 2000;77:3161.
[3] Ajayan PM, Schadler LS, Giannaris C, Rubio A. Adv Mater 2000;12:750.
[4] Flahaut E, Peigney A, Laurent CH, Marliere CH, Chastel F, Rousset A. Acta Mater 2000;48:3803.
[5] Ma RZ, Wu J, Wei BQ, Liang J, Wu DH. J Mater Sci 1998;33:5243.
[6] Zhan GD, Kuntz JD, Wan JW, Mukherjee AK. Nature Mater 2003;2:38.
[7] Seraphin S, Zhou D. Appl Phys Lett 1994;64:2087.
[8] Thess A, Lee R, Nikolaev P, Dai H, Petit P, Robert J, et al. Science 1996;273:483.
[9] Dai H, Rinzler AG, Nikolaev P, Thess A, Colbert DT, Smalley RE. Chem Phys Lett 1996;260:471.
[10] Tohji K, Takahashi H, Shimizu N, Jeyadevan B, Matsuoka I, Saito Y, et al. J Phys Chem 1997;101:1974.
[11] Kataura H, Kumazawa Y, Maniwa Y, Ohtsuka Y, Sen R, Suzuki S, et al. Carbon 2000;38:1691.
[12] Sato Y, Jeyadevan B, Hatakeyama R, Kasuya A, Tohji K. Chem Phys Lett 2004;385:323.
[13] Bachilo SM, Strano MS, Kittrell C, Hauge RH, Smalley RE, Weisman RB. Science 2002;298:2361.
[14] Omori M. Mater Sci Eng A 2000;287:183.
[15] Okuda S, Saito M, Hashida T, Takahashi H. Trans JSME A 1991;57:940.

CHEMISTRY OF MATERIALS

VOLUME 18, NUMBER 18 SEPTEMBER 5, 2006

Communications

Preparation of Single-Walled Carbon Nanotube–Organosilicon Hybrids and Their Enhanced Field Emission Properties

Yutaka Maeda,[†] Yoshinori Sato,[‡] Masahiro Kako,[§] Takatsugu Wakahara,[∥] Takeshi Akasaka,*[,∥] Jing Lu,[⊥] Shigeru Nagase,*[,#] Yumiko Kobori,[†] Tadashi Hasegawa,*[,†] Kenichi Motomiya,[‡] Kazuyuki Tohji,*[,‡] Atsuo Kasuya,[⊗] Dan Wang,[○] Dapeng Yu,[⊥] Zhengxiang Gao,[⊥] Rushan Han,[⊥] and Hengqiang Ye[⊥]

Department of Chemistry, Tokyo Gakugei University, Tokyo 184-8501, Japan, Graduate School of Environmental Studies and Center for Interdisciplinary Research, Tohoku University, Sendai, 980-8579, Japan, Department of Chemistry, The University of Electro-Communications, Tokyo 182-8585, Japan, Center for Tsukuba Advanced Research Alliance, University of Tsukuba, Tsukuba 305-8577, Japan, Mesoscopic Physics Laboratory, Department of Physics, Peking University, Beijing 100871, People's Republic of China, Department of Theoretical Molecular Science, Institute for Molecular Science, Okazaki 444-8585, Japan, and Department of Physics, Capital Normal University, Beijing 100037, People's Republic of China

Received May 11, 2006
Revised Manuscript Received July 17, 2006

Since single-walled carbon nanotubes (SWNTs) were discovered in 1993,[1] their unique physical and electronic properties have attracted considerable interest. SWNTs have been used as field emission sources of field emission display devices because of their unique structures and prominent stability.[2] It is well-known that adsorption of various gases on SWNTs leads to different field emission characteristics. For example, exposure of SWNTs to oxygen gas increases the turn-on voltage and decreases the field emission current,[3] whereas intercalation of Cs atoms decreases the turn-on voltage by a factor of 2.1−2.8 and increases the field emission current by a factor of 10 to the power of 6.[4]

Organosilicon compounds, in which extensive delocalization of σ electrons takes place along the silicon chain, have many unique and interesting electronic properties.[5] In this account, we report novel hybrid materials prepared from SWNTs and organosilicon compounds. Interestingly, the hybrid materials exhibit significantly enhanced field emission efficiency compared with pristine SWNTs.

SWNTs produced by the pulsed laser vaporization method of a metal/carbon target in a furnace at 1100 °C and purified by a previously reported procedure were obtained as toluene suspension from the Tubes@Rice. For the addition of silyl radical, the SWNTs were dispersed in benzene by ultrasonication. Irradiation of a degassed benzene suspension containing SWNTs (2 mg) and 1,1,2,2-tetraphenyl-1,2-di-*tert*-butyl-

* To whom correspondence should be addresseed. E-mail: akasaka@tara.tsukuba.ac.jp (T.A.), nagase@ism.ac.jp (S.N.), tadashi@u-gakugei.ac.jp (T.H.), tohjik@mail.kankyo.tohoku.ac.jp (K.T.).
† Tokyo Gakugei University.
‡ Graduate School of Environmental Studies, Tohoku University.
§ The University of Electro-Communications.
∥ University of Tsukuba.
⊥ Peking University.
Institute for Molecular Science.
⊗ Center for Interdisciplinary Research, Tohoku University.
○ Capital Normal University.

(1) (a) Iijima, S.; Ichihashi, T. *Nature* **1993**, *363*, 603. (b) Bethune, D. S.; Kiang, C. H.; de Vries, M. S.; Gorman, G.; Savoy, R.; Vazquez, J.; Bever, R. *Nature* **1993**, *363*, 605.
(2) (a) de Heer, W. A.; Chatelain, A.; Ugarte, D. *Science* **1995**, *270*, 1179. (b) Saito, Y.; Hamaguchi, K.; Hata, K.; Uchida, K.; Tasaka, Y.; Ikazaki, F.; Yumura, M.; Kasuyam, A.; Nishima, Y. *Nature* **1997**, *389*, 554. (c) Bonard, J.-M.; Salvetat, J.-P.; Stockli, T.; de Heer, W. A. *Appl. Phys. Lett.* **1998**, *73*, 918.
(3) Dean, K. A.; Chalamala, B. R. *Appl. Phys. Lett.* **1995**, *75*, 3017.
(4) Wadhawan, A.; Stallcup, R. E., II; Perez, J. M. *Appl. Phys. Lett.* **2001**, *78*, 108.
(5) (a) Steinmetz, M. G. *Chem. Rev.* **1995**, *95*, 1527. (b) Rappoport, Z., Apeloig, Y., Eds. *The Chemistry of Organosilicon Compounds*; John Wiley & Sons: New York, 1998.

10.1021/cm061100s CCC: $33.50
Published on Web 08/08/2006

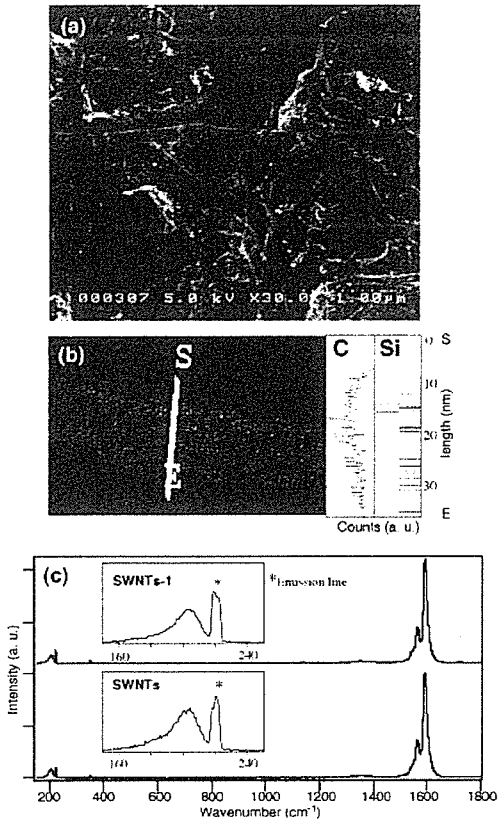

Figure 1. (a) SEM image of SWNTs-**1**. (b) EDS analysis of SWNTs-**1**. (c) Raman spectra of SWNTs and SWNTs-**1**.

1,2-disilane (**1**, 10 mg) with a low-pressure mercury-arc lamp resulted in formation of the silylated SWNTs (SWNTs-**1**). The SWNTs-**1** were collected and washed by toluene to remove residual silicon compounds. The SWNTs on which organosilicon compounds are adsorbed (SWNTs/**1**) were prepared from the ultrasonic treatment of a mixture of 2 mg of SWNTs and 10 mg of organosilicon compounds in 10 mL of benzene at room temperature. SWNTs/**1** were collected by filtration using a membrane filter, washed with benzene to remove free organosilicon molecules, and then dried. The carbene adduct of SWNTs (SWNTs-CH_2) was prepared from the reaction of SWNTs and diazomethane.[6] A SWNTs (50 mg) dispersion in toluene was added to the ether solution of diazomethane (large excess) at 0 °C and then stirred at room temperature under an Ar atmosphere in the dark. The reaction mixture was heated to 100 °C and then was collected and washed by toluene. The diazomethane was prepared from *p*-tolylsulfonylmethynitrosamide and Carbitor by the literature method.[7] (*Diazomethane is toxic and explosive.*)

Figure 1a is a scanning electron microscope (SEM) image of the SWNTs-**1**. SWNTs-**1** are clean and uniformly distributed in the form of bundles. The existence of silicon in the SWNTs-**1** was demonstrated clearly by energy dispersive X-ray spectrometry (EDS) line analysis, as shown in Figure

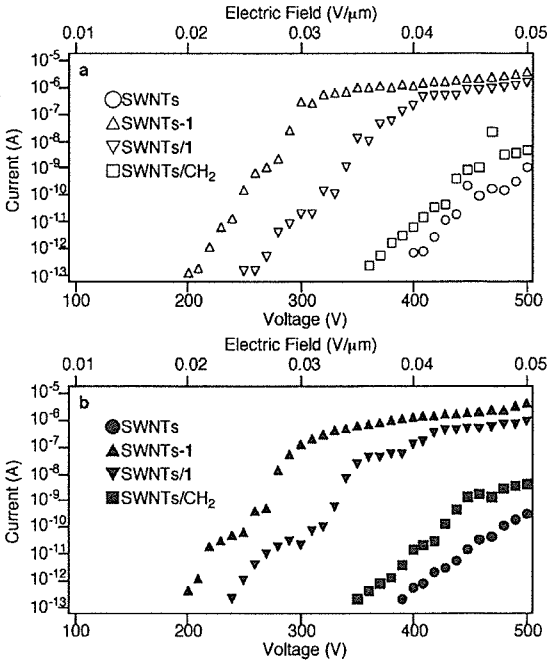

Figure 2. Plots of the field emission current vs voltage of SWNTs, SWNTs-**1**, and SWNTs-CH_2. (a) First scan. (b) Second scan.

1b. Raman spectroscopy is useful for characterizing SWNT features.[8] As shown in Figure 1c, the typical Raman pattern of the SWNTs excited at 488 nm was observed. It shows the well-defined radial breathing mode at 200 cm^{-1}, a strong tangential mode at 1590 cm^{-1}, and a disorder mode with very low intensity at 1350 cm^{-1}. It is well-known that charge-transfer between SWNTs and dopant, such as alkali metals, shifts the tangential modes remarkably.[9] No significant difference in the tangential mode between pristine SWNTs and SWNTs-**1** was observed, although theoretical calculations (see below) reveal that about 0.7−0.8 electron is transferred from SiH_2 to SWNT. It may be due to the small number of silicon substituents on the sidewall of SWNTs bundles.

The field emission currents were measured as a function of applied voltage at a pressure of 1.0×10^{-7} Torr for a spacer of 10 mm between a cathode of the SWNTs tips and an anode of the Faraday cup. Isosceles triangle-shaped SWNTs tips were cut out from the mats of SWNTs, SWNTs-**1**, and SWNTs/**1** using a razor and were fixed on top of hair-pin shaped wires using Ag paste to measure the field emission properties, respectively. The anode was electrically grounded, and the negative bias was applied to the cathode (up to 500 V). Weak and unstable currents were observed for each sample only at the first rising of the voltage around 150−200 V; these suggest removal of adsorbates. Current−voltage ($I-V$) properties were measured from 500 to 0 V.[9] From the $I-V$ characteristics (Figure 2a), the turn-on voltage decreases from 400 to 200 V/0.1 pA by silylation, and the

(6) Chen, J.; Hamon, M. A.; Hu, H.; Chen, Y.; Rao, A. M.; Eklund, P. C.; Haddon, R. C. *Science* **1998**, *282*, 95.
(7) De Boer, H. J.; Backer, H. J. In *Organic Synthesis*; Rabjohnm, N., Ed.; Wiley: New York, 1963; Collective Vol. 4, p 250.
(8) Rao, A. M.; Richter, E.; Bandow, S.; Chase, B.; Eklund, P. C.; Williams, K. A.; Fang, S.; Subbaswamy, K. R.; Menon, M.; Thess, A.; Smalley, R. E.; Dresselhaus, G.; Dresselhaus, M. S. *Science* **1997**, *275*, 187.
(9) Rao, A. M.; Eklund, P. C.; Bandow, S.; Thess, A.; Smalley, R. E. *Nature* **1997**, *388*, 257.

field emission current increases from 10^{-8} to 10^{-6} A at a voltage of 500 V. SWNTs-CH_2 also show a lower gate voltage (350 V/0.1 pA) than SWNTs.[10] These results suggest that the chemical functionalization improves field emission properties of SWNTs significantly. The second measurements of the same SWNT tips showed the result similar to the $I-V$ properties of the first measurements, as shown in Figure 2b.

We have reported that the covalent combination of C_{60} and organosilicon compounds produces a new class of silylfullerene. The combining π and σ conjugated compounds have interesting characteristics, and the silylfullerene has lower oxidation and higher reduction potentials than the analogous carbon substituted derivatives as well as C_{60} itself.[11] This unique electrochemical property is the electron-releasing nature of silicon relative to carbon. In addition to the covalent combination, a noncovalent combination of C_{60} and organosilicon compounds was realized by Wang et al., who reported that doping of fullerene into polysilane enhances its charge-generation efficiency significantly.[12] We compared the field emission properties between SWNTs and the adsorbed adduct (SWNTs/**1**). SWNTs/**1** shows a lower gate voltage (250 V/0.1 pA) than SWNTs, suggesting that the intermolecular $\sigma-\pi$ interaction between SWNTs and the organosilicon compound also enhances effectively the field emission of SWNTs.

To understand the above experimental results, we have studied the interaction of SiH_2 and Si_2H_6 with the semiconducting (10,0) SWNT and that of SiH_2 with the metallic (5,5) SWNT by using local density functional theory. In the case of Si_2H_6-(10,0), a supercell containing double unit cells of the (10,0) SWNT is constructed, while in the case of SiH_2-(5,5), a supercell containing three unit cells of the (5,5) SWNT is constructed. Full geometry optimization was performed for both the atomic positions and lattice lengths by using the ultrasoft pseudopotential plane-wave program,[13] CASTEP,[14] with a cutoff energy of 240 eV. The convergence tolerance of force on each atom is 0.01 eV/Å. Static total energies of the relaxed structures are calculated with a larger 310 eV cutoff energy. An all-electron double numerical atomic orbital basis set[13] is employed to calculate the electronic energy bands. SiH_2 is adsorbed on the sidewall of the (10,0) SWNT (Figure 3a), and the adsorption energies are 2.11, 4.34, and 8.02 eV for one , two, and four SiH_2 groups per super cell, respectively (the corresponding ratio of Si:C is 2.5%, 5%, and 10%, respectively). The band gap of the (10,0) SWNT is reduced from 0.81 to 0.73, 0.53, and 0.23 eV, respectively, as a result of the formation of new bands in the band gap by SiH_2 addition (Figure 3b). Each SiH_2 group induces a new band in the band gap of the nanotube and donates about 0.7−0.8 electrons to the nanotube. Notably, the Fermi level of the (10,0) SWNT is elevated by 0.24, 0.46, and 1.06 eV, respectively, by one, two, and four SiH_2 additions per unit cell, suggesting a corresponding reduction of 0.24, 0.46, and 1.06 eV in the work function (in the first approximation, the work function is equal to the negative Fermi level).[15] Similarly, the Fermi level of the (5,5) SWNT is elevated by 0.10 and 0.50 eV by one and six SiH_2 additions per supercell (the corresponding ratio of Si:C is 1.7% and 10%, respectively). These remarkable reductions in the work function are in agreement with the measured remarkable reduction in turn-on voltage of field emission of SWNT upon silylation.

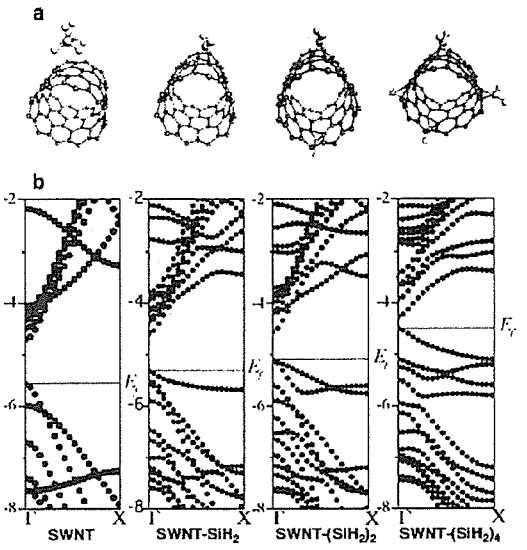

Figure 3. (a) Optimized structures of Si_2H_6-physisorbed (10,0) and SiH_2-adsorbed (10,0) SWNTs with one, two, and four SiH_2 per unit cell. (b) Electronic band structures of pure and SiH_2-adsorbed (10,0) SWNTs with one, two, and four SiH_2 per unit cell.

Covalent functionalization by CH_2 elevates the Fermi level of SWNTs in a less significant way than that by SiH_2. The Fermi level of the (10,0) SWNT is only elevated by 0.59 eV upon four CH_2 additions per unit cell, half the value of SiH_2 addition. This appears qualitatively consistent with the observed smaller enhancement in field emission upon CH_2 addition than organosilicon addition as shown in Figure 1. Si_2H_6 is physisorbed on the surface of the nanotube (Figure 3a) with an adsorption energy of 0.19 eV. The shortest atom-to-atom distance between Si_2H_6 and the (10,0) SWNT is 2.88 Å. No significant shift of the Fermi level is found at this concentration, but 0.01 electrons are transferred from Si_2H_6 to the nanotube. If the concentration of Si_2H_6 is increased by a factor of 10, the number of transferred electrons would be increased to about 0.1. These transferred electrons are likely to fill the conduction band rigidly and elevate the Fermi level as in the case of Cs doping.[16] Therefore, the mechanism of enhanced field emission upon physisorption of organosilicon can be understood in terms of a simple electron-transfer picture.

Extensive delocalization of σ electrons takes place along the silicon chain, giving rise to many interesting electronic

(10) (a) Saito, Y.; Hamaguchi, K.; Nishino, T.; Hata, K.; Tohji, K.; Kasuya, A.; Nishina, Y. *Jpn. J. Appl. Phys.* **1997**, *36*, L1340−L1342. (b) Saito, Y.; Uemura, S. *Carbon* **2000**, *38*, 169−182.
(11) (a) Suzuki, T.; Maruyama, Y.; Akasaka, T.; Ando, W.; Kobayashi, K.; Nagae, S. *J. Am. Chem. Soc.* **1994**, *116*, 1359. (b) Maeda, Y.; Rahman, R. M. A.; Wakahara, T.; Kako, M.; Okamura, M.; Sato, S.; Akasaka, T.; Kobayashi, K.; Nagase, S. *J. Org. Chem.* **2003**, *68*, 6791.
(12) Wang, Y.; West, R.; Yuan, C. H. *J. Am. Chem. Soc.* **1993**, *115*, 3844.
(13) Vanderbit, D. *Phys. Rev. B.* **1990**, *41*, 7892.
(14) Milman, V.; Winkler, B.; White, J. A.; Pickard, C. J.; Payne, M. C.; Akhmatskaya, E. V.; Hobes, R. E. *J. Quantum Chem.* **2000**, *77*, 895.
(15) Delley, B. *J. Chem. Phys.* **2000**, *113*, 7756.
(16) Zhao, J.; Han, J.; Lu, J. P. *Phys. Rev. B* **2002**, *65*, 193401.

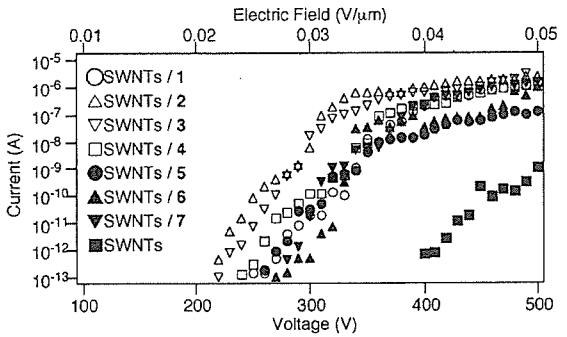

Figure 4. Plots of the field emission current vs voltage.

properties. For example, because of this σ-conjugation, the ionization potential is very sensitive to the silicon backbone. We attempted to expand this approach to other oligosilanes and polysilanes. The $I-V$ characteristic of the absorptive adducts SWNTs/**1**−**7** under the same condition also has an enhanced emission when compared to pristine SWNTs, as shown in Figure 4. All organosilicon compounds have improved the filed emission property of SWNTs. But the field emission property of these hybrid materials was not sensitive to the oxidation potential of the organosilicon compounds (Table 1). It was reported that not only oxidation potential but also the structures of the organosilicon compounds are important for the charge-generation efficiency of fullerene toward polysilane.[12]

In conclusion, the SWNT−organosilicon hybrids were prepared. In accordance with the significantly reduced work function found by density functional theory calculations, silylation of SWNTs significantly increases the field emission properties of SWNTs. The physisorption of organosilicon compounds on the surface of SWNTs is also effective for improvement of the field emission properties of SWNTs. Unlike the classical alkali metal doping, the hybrid materials of SWNTs with organosilicon compounds are stable under oxygen. This simple modification suggests a great potential industrial utilization as building blocks for field emission sources.

Table 1. (a) Turn-On Voltages for Various Film Field Emitters and (b) the Anodic Peak Potentials of Organosilicon Compounds[a]

a. Turn-On Voltages

compound	V (V)	compound	V (V)
SWNTs/*c*-$(Et_2Si)_5$ (**2**)	220	SWNTs/$Ph(SiPh_2)_3Ph$ (**5**)	260
SWNTs/$(Hex_2Si)_n$ (**3**)	220	SWNTs/*c*-$(Ph_2Si)_5$ (**6**)	270
SWNTs/$Ph_3Si(SiMe_2)_2$-$SiPh_3$ (**4**)	240	SWNTs/$(PhMeSi)_n$ (**7**)	280
SWNTs/$(t$BuPh$_2$Si$)_2$ (**1**)	250	SWNTs	400

b. Anodic Peak Potentials[a]

compound	V vs SCE	compound	V vs SCE
c-$(Et_2Si)_5$ (**2**)	1.62	$Ph(SiPh_2)_3Ph$ (**5**)	1.74
$(Hex_2Si)_n$ (**3**)	1.60[b]	*c*-$(Ph_2Si)_5$ (**6**)	1.61
$Ph_3Si(SiMe_2)_2SiPh_3$ (**4**)	1.76	$(PhMeSi)_n$ (**7**)	1.00[b]
$(t$BuPh$_2$Si$)_2$ (**1**)	1.90		

[a] The first anodic peak potentials scan rate; 50 mV/s, 0.1 M TBAP of a CH_2Cl_2 solution. [b] Miller, R. D.; Michl, J. *Chem. Rev.* **1989**, *89*, 1359.

Acknowledgment. This work was supported in part by the Kurata Memorial Hitachi Science and Technology Foundation and NEDO of Japan, and by a Grant-in-Aid, Nanotechnology Support Project and the 21st Century COE Program from MEXT of Japan. This work was also supported by NSFC and national 973 projects from MOST of China.

Supporting Information Available: Characterization of SWNTs-CH_2 (PDF). This material is available free of charge via the Internet at http://pubs/acs.org.

CM061100S

Relation of the Number of Cross-Links and Mechanical Properties of Multi-Walled Carbon Nanotube Films Formed by a Dehydration Condensation Reaction

Shin-ichi Ogino,[†] Yoshinori Sato,*[,†] Go Yamamoto,[‡,§] Kenichiro Sasamori,[||] Hisamichi Kimura,[||] Toshiyuki Hashida,[§] Kenichi Motomiya,[†] Balachandran Jeyadevan,[†] and Kazuyuki Tohji[†]

Graduate School of Environmental Studies, Tohoku University, Sendai 980-8579, Japan, Institute of Fluid Science, Tohoku University, Sendai 980-8577, Japan, Fracture and Reliability Research Institute, Graduate School of Engineering, Tohoku University, Sendai 980-8579, Japan, and Institute for Materials Research, Tohoku Univesity, Sendai 980-8577, Japan

Received: July 5, 2006; In Final Form: August 27, 2006

Multi-walled carbon nanotube (MWCNT) films were prepared by employing a condensation reaction utilizing 1,3-dicyclohexylcarbodiimide (DCC) to cross-link each MWCNT with carboxylic acid and hydroxyl groups. Morphological changes in the resultant MWCNT films were monitored using scanning electron microscopy and showed that the MWCNTs were randomly intertwined in the films. The prepared MWCNT films were 17 mm in diameter and 20 μm in thickness, and the apparent density was 0.59 g/cm^3. Fourier transform-infrared spectroscopy confirmed that each MWCNT modified with carboxylic acid and hydroxyl groups was cross-linked through the ester bond. It was found that the ratio of the number of ester cross-links and carbon atoms of the nanotubes per unit apparent volume (cm^3) of condensed-MWCNT films was 5.27×10^{-3} using thermogravimetric analysis (TGA). The tensile strength and Vickers hardness of condensed-MWCNT films achieved an average of 15 and 9.2 MPa, respectively, and were greater than those of free-standing MWCNT films without ester bond.

Introduction

Carbon nanotubes (CNTs) films have been utilized in the form of sensor electrodes[1] and actuators.[2] Multi-walled carbon nanotubes (MWCNTs) are made up of more than one layer that form concentric graphene tubes that possess metallic properties and high mechanical strength. However, it is more difficult to form MWCNT films in comparison to forming single-walled carbon nanotube (SWCNT) films[3−5] since MWCNTs are more rigid due to the large number of concentric graphene tubes. To date, researchers have reported on the chemical polymerization of short carboxylic SWCNTs into "rings"[6] or "large strands"[7] by application of a condensation reaction. Ester bonds can be synthesized by a dehydration condensation reaction of a carboxylic group with a hydroxyl group in the presence of a dehydration−condensation-coupling agent. This reaction is also useful in generating nanotube assemblies such as films in an effort to solve the aforementioned problem. Here, we report on the ester cross-linking of MWCNTs into thin films by employing a dehydration condensation reaction esterification with the assistance of 1,3-dicyclohexylcarbodiimide (DDC) and estimate the number of ester cross-links involving MWCNTs and examine the mechanical properties such as tensile strength and Vickers hardness.

Experimental Section

The MWCNTs used in this study had been synthesized by the chemical vapor deposition (CVD) method and were obtained from NanoLab, Inc. The purity was about 80 wt %, and impurities included amorphous carbon, Fe, Mo, Cr, and Al. The diameter was in the range between 20 and 40 nm, and the length was in the range between 500 nm and 5.0 μm. A 100 mg amount of the soot was burned in air at 773 K for 90 min, and the burnt soot was then introduced into a flask containing 6 M HCl to dissolve the metals (purified-MWCNTs). Following this, the acid solution was filtered using a membrane filter, and 500 mg of the filtered cake was transferred into a flask containing 500 mL of 6.8 mol/L HNO_3. The mixture was sonicated for 5 min and then refluxed with stirring at 373 K for 16 h to modify surface carboxylic acid and hydroxyl and carbonyl groups.[8,9] The resultant suspension was filtered using a membrane filter, and the filtered cake was dried in oven at 333 K for 24 h. The resultant sample, referred to as "hydrophile-MWCNTs", consisted of the following: C, 99.498 wt %; Al, 0.159 wt %; Fe, 0.321 wt %; Mo, 0.019 wt %; and Cr, 0.003 wt % as determined by ICP-OES and found to be highly pure.[10] The method employed to generate the MWCNT films was as follows: 100 mg of hydrophile-MWCNTs was introduced into a flask containing *N*,*N*-dimethylformamide (DMF) and sonicated for 60 min. Following this, the suspension was stirred at room temperature for 24 h to effectively disperse the nanotubes. A 20 mL aliquot of the resultant suspension was removed and filtered using a PTFE membrane filter with a pore size of 0.1 μm. After filtering the suspension, the cake was thoroughly washed with ethanol to remove DMF. The cake adhered to the PTFE membrane was then sandwiched between Teflon plates and dried at room temperature for over 12 h under pressure at 1.6×10^3 Pa. The resultant sample, referred to as "hydrophile-MWCNT film", was then removed from the PTFE membrane. The method employed to generate MWCNT films assembled by a condensation reaction was as follows: hydrophile-MWCNT films were placed on the Teflon plate inset at the base of a glass Petri dish. A 20 mL aliquot of DMF in which 20 mg of

* Corresponding author. Telephone/Fax: +81-22-795-7392. E-mail: hige@buckyl.kankyo.tohoku.ac.jp.
[†] Graduate School of Environmental Studies.
[‡] Institute of Fluid Science.
[§] Graduate School of Engineering.
[||] Institute for Materials Research.

10.1021/jp0642387 CCC: $33.50
Published on Web 10/26/2006

DCC was added and was gently poured into the dish. The dish was then sealed in the flask placed in a water bath set at 333 K, and the reaction allowed to proceed for 24 h. Following this, DMF was removed from the dish, and DCC and DMF were thoroughly removed using ethanol. The sample was allowed to dry at room temperature for over 24 h, and the resultant film was referred to as "condensed-MWCNT film". In an effort to estimate the apparent density of the resultant films, film weight and size were measured using an analytical electrobalance (GR-202; A & D Co. Ltd., Japan) and universal profile projector (PJ300H; Mitutoyo Co., Japan) for length and width determinations and a high-precision microscale (M200; Mitutoyo Co., Japan) for thickness determinations. The sample was characterized using scanning electron microscopy (SEM; S-4100, Hitachi, Japan), transmission electron microscopy (TEM; HF-2000, Hitachi, Japan), Fourier transform-infrared spectroscopy (FT-IR; Avatar 360, Thermo Electron Co. Ltd., USA), inductively coupled plasma optical emission spectroscopy (ICP-OES; IRIS Advantage DUO, Thermo Electron), and high-resolution thermogravimetric analysis (dynamic TG-8210, Thermo Mass, Rigaku Co. Ltd., Japan). The tensile mechanical properties of MWCNT films were determined using INSTRON 4310. Tensile tests were conducted on 2.0 mm wide and 20 μm thick specimens at a gauge length of 10 mm and a strain rate of 0.2 mm/min. Micro Vickers hardness tests were measured using an MVK-VL hardness tester with a diamond Vickers indenter (Akashi, Japan). The indentation parameters consisted of a 98.07 mN load with a dwell of 15 s.

Results and Discussion

An image of a condensed-MWCNT film and a typical SEM photograph of its surface are shown in Figure 1. The condensed-MWCNT films were 17 mm in diameter and 20 μm in thickness (Figure 1a), and the apparent density was 0.59 g/cm^3. Although films were somewhat brittle, they could fashion into various shapes. The hydrophile-MWCNTs possessed an average length of 1.5 μm with a curved shape and each MWCNT randomly intertwined in the condensed-MWCNT films (Figure 1b).

The presence of functional groups on the samples was established using IR spectroscopy with transmission method (KBr pellet). The IR spectrum of carbon nanotubes with a higher defect concentration is well-known as having a broader band at 1200 cm^{-1} that is assigned to a signal derived from the carbon skeleton.[11-13] As the broader band around 1200 cm^{-1} appeared in the IR spectrum of raw- or purified-MWCNTs, we confirmed that the degree of graphitization for the used MWCNTs was lower than that of the purified MWCNTs synthesized by arc-discharge method[14] (Figure S1 of the Supporting Information). From the IR spectra of the hydrophile-MWCNT films and condensed-MWCNT films (Figure 2), the band present at 1584 cm^{-1} in the two spectra is associated with the stretching vibration of the aromatic C=C group.[15] In the case of hydrophile-MWCNT films, the small band at 1725 cm^{-1} was assigned to the stretching vibration of the C=O carboxylic acid and carbonyl, while bands at 3130 and 3440 cm^{-1} correspond to the stretching vibration of the O−H carboxyl, hydroxyl, and phenolic groups. The band at 1404 cm^{-1} was assigned to the C−O symmetrical stretching vibration of carboxylate ions or O−H bending deformation vibration in carboxylic acid, hydroxyl, and phenolic groups. The broader band range from 1050 to 1194 cm^{-1} was assigned to the C−O stretching vibration of hydroxyl and phenol groups.[16] The surface of the hydrophile-MWCNT films is considered to be modified through carboxylic acid and hydroxyl groups. On the other hand, following

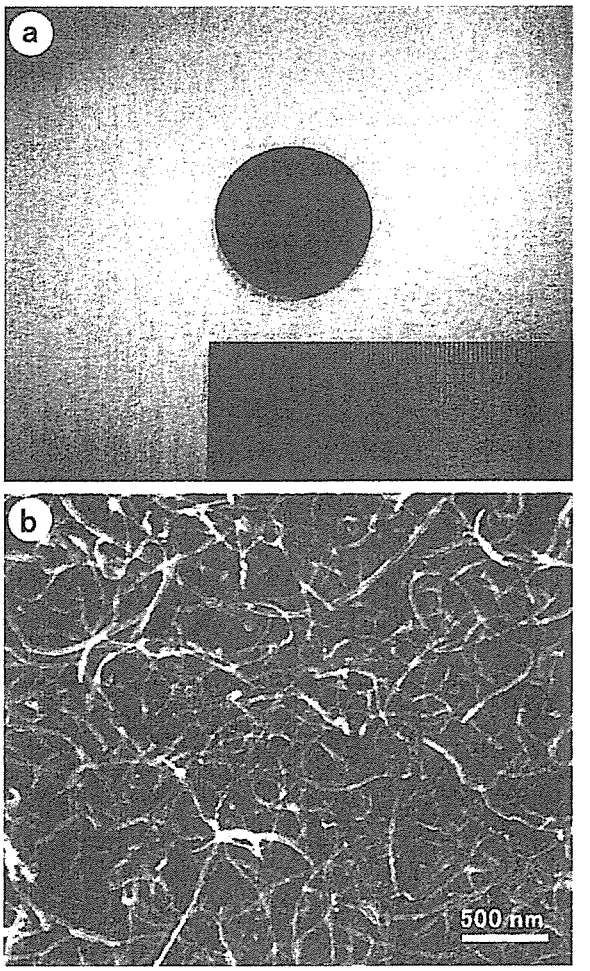

Figure 1. (a) Typical image of condensed-MWCNT films. (b) SEM image of the surface of condensed-MWCNT films.

dehydration condensation, the band around 3440 cm^{-1} representing O−H stretching of carboxylic acid groups, the peak at 1404 cm^{-1} representing the C−O symmetrical stretching vibration of carboxylate ions or O−H bending deformation vibration of carboxylic acid, hydroxyl, and phenolic groups all decrease. Furthermore, the half-maximum full-width of the broader peak at 1221 cm^{-1} is narrow and may be accounted for by the presence of stretching vibrational modes of ester groups (O−C−O). Although the 1725 cm^{-1} peak comprises unreacted carboxylic acids and ketones in condensed-MWCNT films, the stretching vibration of the C=O moiety in ester groups (C=O(−O)−C) is thought to be represented by this peak. The aforementioned speculations suggest that the carboxylic acid and hydroxyl groups on the nanotube surface are modified through conversion into ester bonds with subsequent loss of water (H_2O) and represent ester product formation by a condensation reaction. The ester bond in condensed-MWCNT films would provide for the possibility of cross-linking as well as for enhanced intertube interactions. However, as both C=O (1725 cm^{-1}) and C−O (1221 cm^{-1}) stretching bands associated with the ester group are very small, the yield of ester bonds might be low.

Additionally, evidence of covalent functionalization on the surface of the carbon nanotubes was provided by Raman spectroscopy. The D-band (1350 cm^{-1}) intensity increased with increasing covalent functionalization of the nanotube. The I_D/I_G of purified-MWCNTs was found to be 0.868. On the other